Published in IET Microwaves, Antennas & Propagation
Received on 11th September 2011
Revised on 28th May 2012
doi: 10.1049/iet-map.2011.0436

ISSN 1751-8725

Ungrounded composite right-/left-handed metamaterials: design, synthesis and applications

M. Rafael Booket[1] *M. Veysi*[2] *Z. Atlasbaf*[1] *A. Jafargholi*[2]

[1]*School of Electrical and Computer Engineering, Trabiat Modares University, Tehran, Iran*
[2]*Electrical Engineering Department, K. N. Toosi University of Technology, Tehran, Iran*
E-mail: jafargholi@ee.kntu.ac.ir

Abstract: The design of ungrounded meander line inductors (UMIs) and ungrounded interdigital capacitors (UICs) employed in the practical realisation of a planar ungrounded composite right-/left-handed (UCRLH) metamaterial is presented. Accurate lumped-element circuit models are proposed based on partial element theory and conformal mapping method. New and accurate analytical design formulas, for both the UMI and the UIC at very high frequency and ultra high frequency bands are derived and successfully validated through a proper comparison with the existing measurement data and the results obtained with the full wave method of moments. Further insight is sought through the investigation of the resonance mechanism of a printed dipole antenna loaded with UCRLH metamaterial cells. A prototype of the loaded dipole is fabricated to confirm and validate the theoretical calculations. The experimental results are found to be in good agreement with the theoretical calculations.

1 Introduction

Current advancements in wireless or mobile communication systems demonstrate the need for low cost, small size and more reliable microwave components. In this regard, lumped-element components have received much interest owing to their small size, low fabrication cost and wide-band characteristics [1, 2]. Interdigital capacitors [3] and meander line inductors [4, 5] are two important categories of lumped-element components. These two main categories have been widely applied in the practical realisation of metamaterials. The microstrip (one-dimensional) implementation of left-handed (LH) metamaterials constituted of series interdigital capacitors and shunt stub inductors was first proposed by Caloz *et al.* in 2002 [6, 7] and widely used in various applications [8, 9]. It was also demonstrated in [10] that as an electromagnetic wave propagates along a metamaterial (MTM) structure realised by lumped element components, the related voltages and currents induce other parasitic effects. The parallel-plate voltage gradients between the upper conductors and the ground plane cause a shunt capacitance. In addition, the currents flowing along the digits of the interdigital capacitor induce magnetic fluxes which in turn result in a series inductance. As a result, the term composite right-/left-handed (CRLH) metamaterial is used to describe the exact nature of practical LH media [10]. The CRLH metamaterials comprised of a periodic arrangement of grounded meander line inductors and grounded interdigital capacitors can be designed based on existing analytical formulas [3, 4, 11]. Grounded interdigital capacitors and their application to lumped element microwave integrated circuits have been studied in detail in [3]. The equivalent circuit models for grounded single-side meander line inductors (SSMIs) and double-side meander line inductors (DSMIs) have been also proposed in [4] and [5], respectively.

This paper introduces a planar ungrounded CRLH (UCRLH) metamaterial composed of a periodic arrangement of ungrounded interdigital capacitors (UICs) and ungrounded meander line inductors (UMIs). Although the concepts of the UICs and UMIs are not new and have been used in many practical applications [12–14], to the best of the authors' knowledge, there are no papers reporting ideal lumped-element circuit models and design formulas for these kinds of microwave components. In this paper, accurate lumped-element circuit models and analytical formulas for UICs and UMIs are proposed, based on the partial elements theory and the conformal mapping method, to predict the behaviour of UCRLH metamaterials. These ideal lumped element models together with the closed form expressions for the capacitors and inductors have also been used to study the quality factors, Q, and the resonance frequencies of these microwave components. The effects of the design parameters of the UICs and UMIs on their corresponding capacitances and inductances are also investigated to obtain engineering guidelines for UCRLH metamaterial designs. The analytical results have been successfully validated through a comparison with existing measurement data and those obtained with the full-wave method of moments (MoM) procedure. An example of a printed dipole antenna loaded with UCRLH metamaterials is presented to demonstrate the capability of the UCRLH metamaterials in antenna miniaturisation. The simulations were performed with Agilent's advanced design system (ADS) based on the full-wave MoM analysis.

2 Ungrounded meander-line inductors

Since the metamaterial inclusions are supposed to be very small compared to the operating wavelength, a quasi-static model can be used to describe the electromagnetic behaviour of the inclusions. A UMI consists of n turns of copper strips printed on top of an ungrounded dielectric substrate. A UMI composed of two turns of copper strips together with its equivalent circuit representation is depicted in Fig. 1. As the number of meander line turns increases, the equivalent inductance and capacitance increase, which in turn results in a lower resonant frequency. Here, the UMI is printed on a dielectric substrate with a thickness h and dielectric constant ε_r. It is evident that in the quasi-static limit, the current flows through the meander line as illustrated in Fig. 1*a*. To simplify the discussion, a logical approximation is to neglect some higher order effects, which have, in any case, a negligible influence in the calculation of the resonant frequency of the UMIs. Efficient analytical formulas for the inductance and capacitance of the UMI are provided in the following subsections.

2.1 Analytical formula for L_{UMI}

In addition to the self-inductance of each segment of UMI, mutual inductances between the adjacent segments have to be considered in the calculation of the overall inductance of the UMI. When the two adjacent segments are excited in their fundamental mode, the sign of mutual inductance can be either -1 or $+1$, depending on the current directions. Considering the large number of meander line turns, the analysis of the UMI requires a further extension of the theory presented in [15–17]. From the current flow schematically illustrated in Fig. 1*a*, it is revealed that the self-inductors of the adjacent segments are all connected in series. In order to simplify the discussion, we assume that the strip width, W, the strip thickness, T and the separation distance between two adjacent parallel strips, S, do not vary from one turn to another. First, the expression of the total self-inductance, given by the series of the self-inductances associated with each separated segment, is derived. The UMI is generally composed of two orthogonal segments, the self-inductances of which are found to be [16] (see (1))

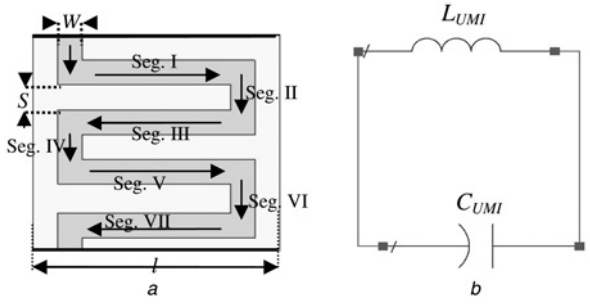

Fig. 1 *Ungrounded meander line inductors*

a Schematic of the two turns UMI
b Quasi-static equivalent circuit of the UMI shown in *a*

where

$$w = W/l, \quad t = T/l$$

$$r = \sqrt{w^2 + t^2}, \quad \alpha_\omega = \sqrt{\omega^2 + 1}$$

$$\alpha_t = \sqrt{t^2 + 1}, \quad \alpha_r = \sqrt{\omega^2 + t^2 + 1}$$

$$\sinh^{-1}(x) = \ln(x + (1 + x^2)^{0.5})$$

In all cases, the strip thickness is fixed at 0.035 mm. The mutual inductance between every two parallel segments is derived by extending the theory presented in [17]

$$\begin{aligned}\text{Mutual}\ (D) = &\left[\frac{1}{2}(L\,\text{self}_{D+W} + L\,\text{self}_{D-W}) - L\,\text{self}_D\right] \\ &\times \left(\frac{D}{W}\right)^2 + (L\,\text{self}_{D+W} - L\,\text{self}_{D-W})\left(\frac{D}{W}\right) \\ &+ \frac{1}{2}(L\,\text{self}_{D+W} - L\,\text{self}_{D-W}) \qquad (2)\end{aligned}$$

$$\begin{aligned}\frac{L\text{self}}{\ell} = \frac{2\mu}{\pi}\Bigg\{ &0.25\left[\frac{1}{w}\sinh^{-1}\left(\frac{w}{\alpha_t}\right) + \frac{1}{t}\sinh^{-1}\left(\frac{t}{\alpha_w}\right) + \sinh^{-1}\left(\frac{1}{r}\right)\right] \\ &+ \frac{1}{24}\left[\begin{array}{l} \frac{t^2}{w}\sinh^{-1}\left(\frac{w}{t\alpha_t(r+\alpha_r)}\right) + \frac{w^2}{t}\sinh^{-1}\left(\frac{t}{w\alpha_w(r+\alpha_r)}\right) \\ + \frac{t^2}{w^2}\sinh^{-1}\left(\frac{w^2}{tr(\alpha_t+\alpha_r)}\right) + \frac{w^2}{t^2}\sinh^{-1}\left(\frac{t^2}{wr(\alpha_w+\alpha_r)}\right) \\ + \frac{1}{w^2}\sinh^{-1}\left(\frac{wt^2}{\alpha_t(\alpha_w+\alpha_r)}\right) + \frac{1}{tw^2}\sinh^{-1}\left(\frac{tw^2}{\alpha_w(\alpha_t+\alpha_r)}\right) \end{array}\right] \\ &- \frac{1}{6}\left[\frac{1}{wt}\tan^{-1}\left(\frac{wt}{\alpha_r}\right) + \frac{t}{w}\tan^{-1}\left(\frac{w}{t\alpha_r}\right) + \frac{w}{t}\tan^{-1}\left(\frac{t}{w\alpha_r}\right)\right] \\ &- \frac{1}{60}\left[\begin{array}{l} \frac{(\alpha_r + r + t + \alpha_t)t^2}{(\alpha_r + r)(r + t)(t + \alpha_t)(\alpha_t + \alpha_r)} \\ + \frac{(\alpha_r + r + w + \alpha_w)w^2}{(\alpha_r + r)(r + w)(w + \alpha_w)(\alpha_w + \alpha_r)} \\ + \frac{(\alpha_r + \alpha_w + 1 + \alpha_t)}{(\alpha_r + \alpha_w)(\alpha_w + 1)(1 + \alpha_t)(\alpha_t + \alpha_r)} \end{array}\right] \\ &- \frac{1}{20}\left[\frac{1}{r + \alpha_r} + \frac{1}{\alpha_w + \alpha_r} + \frac{1}{\alpha_t + \alpha_r}\right]\Bigg\} \qquad (1)\end{aligned}$$

doi: 10.1049/iet-map.2011.0436

where D ($D = S + W$) denotes the distance between the centres of two parallel segments, and Lself is the self inductance given by (1), with the subscript denoting the thickness of the segment (T in (1)). As the separation distance between the parallel segments is increased, the mutual inductance decreases significantly. As a result, the mutual inductances between just two closely spaced segments [e.g. (Segments I and III), (Segments I and V), (Segments II andIV) and (Segments II VI)] should be considered in the calculations. The mutual inductances between other segments, which are spaced far apart, are so small so that they can be neglected. The general expression for the total mutual inductance is then given by

$$M_{\text{total}} = \sum_{i=1}^{2n-1} (-1)^i 2(2n - (i-1))\text{Mutual}(i \times D) \quad (3)$$

where n is the number of meander line turns, and Mutual(i D) is the mutual inductance between two parallel segments separated by a distance i D, given by (2). The total inductance of the UMI is, therefore given by

$$L_{\text{UMI}} = Ls_{\text{total}} \pm M_{\text{total}} \quad (4)$$

where Ls_{total} is the total self inductance of the meander line, and M_{total} is the total mutual inductance given by (3). The obtained analytical formulas relevant to the inductance of the UMI can be validated through a comparison with the existing measurement data reported in [4] for a grounded meander line conductor. To analytically calculate the total inductance of the grounded meander line, it should be pointed out that the ground plane provides a return path for the current based on the image theorem. As a result, the self and mutual inductances associated with the image segments as well as the mutual inductances between the segments and their images effectively contribute to the total inductance of the grounded meander line inductor. The analytical results for the inductance of the grounded meander line inductor (MI) are therefore obtained from the formulas for the UMIs. In all cases, the thickness of the grounded dielectric is fixed at $h = 1.5$ mm. Table 1 compares the analytical results with the existing measurement data [4] for several grounded MIs. As can be seen the agreement between the analytical results and measurement ones is reasonable. It should be pointed here out that only some of the comparative results are shown in Table 1 for the sake of brevity. The effects of design parameters of the UMI on the value of the L_{UMI} are also investigated in order to obtain some engineering guidelines for the meander line inductor designs. The total inductances

Table 1 Analytical results for the inductance of the grounded MIs as compared to the existing measurement data

No.	Turns	l, mm	W, mm	S, mm	L_{measured}, nH	$L_{\text{analytical}}$, nH
1	4	10	0.6	0.4	27.6	26.229
2	4	10	0.8	0..4	25.3	24.069
3	4	10	1.0	0.4	22.6	22.535
4	2	10	2.0	0.4	9.89	9.2498
5	6	8	0.7	0.8	35.7	33.326
6	6	8	0.9	0.8	32.1	30.200
7	2	10	1.0	1.0	17.1	13.135
8	2	15	1.0	1.0	23.5	21.055
9	2	20	1.0	1.0	27.2	29.473
10	4	10	0.4	2.0	45.8	44.152

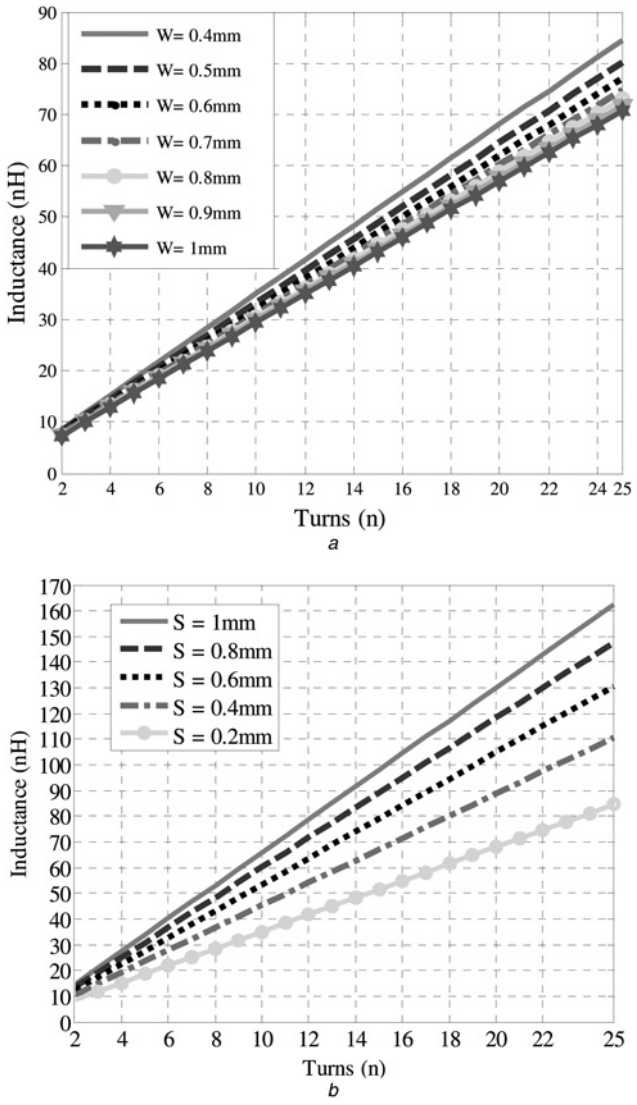

Fig. 2 *Total inductance of UMI as a function of the number of UMI turns, n*

a For different strip widths; $S = 0.2$ mm and $l = 15$ mm
b For different separation distances; $W = 0.4$ mm and $l = 15$ mm

of L_{UMI} as a function of the meander line turns for different separation distances/strip widths are depicted in Fig. 2. It is observed that when the number of meander line turns is increased, the inductance value increases. Moreover, for a constant number of meander line turns, the inductance value increases as the separation distance increases or strip width decreases.

2.2 Analytical formula for C_{UMI}

The capacitance of the UMI is calculated by the conformal mapping method. The schematic of three parallel strips printed on a dielectric substrate with a thickness h and dielectric constant ε_r is shown in Fig. 3. The corresponding air-gap capacitors and dielectric-gap capacitors are also labelled in Fig. 3. Since two adjacent parallel strips with reverse currents act as a co-planar strip (CPS) line in its odd mode, the air-gap capacitor can be determined as

$$C_{ga1} = \frac{\varepsilon_0 K(k_1')}{2K(k_1)} \quad (5)$$

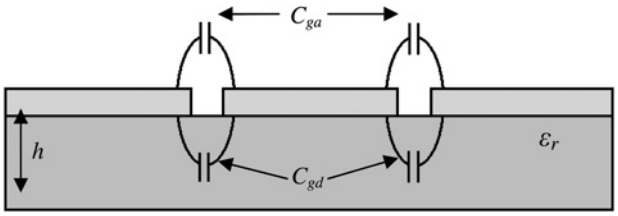

Fig. 3 *Side view of three parallel strips together with the corresponding gap-capacitors*

where $K(k)$ and $K(k')$ denote, respectively, the elliptic function and its complementary, indexes k, and k' are

$$k_1 = S/(S+2W), \quad k_1' = \sqrt{(1-k_1^2)} \tag{6}$$

where W and S are the strip width and the distance between two adjacent strips, respectively.

Following the same methodology, the dielectric-gap capacitor then becomes

$$C_{\text{gd1}} = (\varepsilon_0 \varepsilon_{\text{eff}\,1}/\pi)\ln(\coth(0.25\pi S/h)) \tag{7}$$

where

$$\varepsilon_{\text{eff1}} = 0.5(\varepsilon_r+1)\left(\tanh\left(1.785\log\left(\frac{h}{W}\right)+1.75\right)\right) + \left(k_1\frac{W}{h}\right)(0.04-0.7k_1+0.01(1-0.1\varepsilon_r)(0.25+k_1)) \tag{8}$$

Considering the current flow illustrated in Fig. 1*a* and the voltage distribution, it can be concluded that the distributed capacitors of the adjacent meander line turns are all connected in parallel. However, each turn, itself, consists of two equal capacitors connected in series. As a result, the total gap capacitance of a UMI, is determined by

$$C_{\text{g1}} = (2N-1)(l+s)(C_{\text{ga1}}+C_{\text{gd1}})/2 \tag{9}$$

A correction factor should also be added to the right-handside of (9) to account for the effects of the fields of neighbouring strips on the gap-capacitors. Considering this correction factor, the total capacitance of the N turn meander line inductor then becomes

$$C_{\text{UMI}} = C_{\text{g1}} + C_{\text{correct}} \tag{10}$$

where

$$C_{\text{correct}} = -(C_{\text{g2}}+C_{\text{g3}})$$

and

$$\begin{aligned}
C_{\text{g2}} &= 2(N-1)(l+S)(C_{\text{ga2}}+C_{\text{gd2}})/2\\
C_{\text{ga2}} &= \varepsilon_0 K(k_2')/(2K(k_2))\\
C_{\text{gd2}} &= (\varepsilon_0\varepsilon_{r\,\text{eff}\,2}/\pi)\log(\coth(0.25\times\pi\times(2s+W)/h))\\
k_2 &= ((2s+W)/h)/((2s+W)/h+2W/h)\\
k_2' &= \sqrt{(1-k_2^2)}\\
\varepsilon_{r\,\text{eff}\,2} &= 0.5\times(\varepsilon_r+1)(\tanh(1.785\log 10(h/W)+1.75)\\
&\quad +(k_2W/h)(0.04-0.7k_2+0.01\\
&\quad \times(1-0.1\varepsilon_r)(0.25+k_2)))\\
C_{\text{g3}} &= (2N-3)(l+S)(C_{\text{ga3}}+C_{\text{gd3}})/2 \quad \text{for } N>1\\
C_{\text{ga3}} &= \varepsilon_0 K(k_3')/(2K(k_3))\\
C_{\text{gd3}} &= (\varepsilon_0\varepsilon_{r\,\text{eff}\,3}/\pi)\log(\coth(0.25\times\pi\times(3s+2W)/h))\\
k_3 &= ((2s+W)/h)/((2s+W)/h+2W/h)\\
k_3' &= \sqrt{(1-k_3^2)}\\
\varepsilon_{r\,\text{eff}\,3} &= 0.5\times(\varepsilon_r+1)(\tanh(1.785\log 10(h/W)+1.75)\\
&\quad +(k_3W/h)(0.04-0.7k_3+0.01\\
&\quad \times(1-0.1\varepsilon_r)(0.25+k_3)))
\end{aligned} \tag{11}$$

In the above equations, h and ε_r are, respectively, the thickness and dielectric constant of the ungrounded substrate. The total capacitances of L_{UMI} as a function of the meander line turns for different separation distances/strip widths are depicted in Fig. 4. As can be seen, when

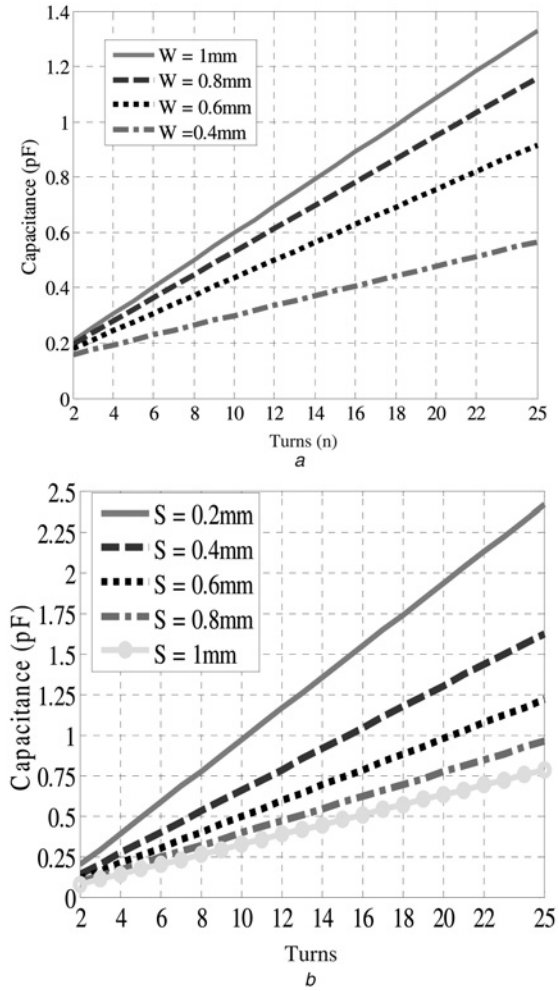

Fig. 4 *Total capacitance of UMI as a function of the number of UMI turns, n*

a For different strip widths; $S = 0.2$ mm, $\varepsilon_r = 3.38$ and $l = 15$ mm
b For different separation distances; $W = 0.4$ mm, $\varepsilon_r = 3.38$ and $l = 15$ mm

doi: 10.1049/iet-map.2011.0436

the number of meander line turns is increased, the capacitance value increases. Moreover, for a constant number of meander line turns, the capacitance value increases as the strip width increases or separation distance decreases.

Table 2 compares the analytical results for the capacitance with the ADS simulation results for several UMIs. As can be seen the agreement between the analytical results and simulation is reasonable.

According to (4) and (10), the resonant frequency of the UMI can be expressed as

$$f_{\mathrm{res_{UMI}}} = \frac{1}{2\pi\sqrt{L_{\mathrm{UMI}}C_{\mathrm{UMI}}}} \tag{12}$$

In order to validate the proposed circuit model of the UMI, some comparisons between the ADS and analytically predicted resonant frequencies have been performed and presented in Fig. 5. As can be seen, the agreement between the quasi-static model and the ADS simulated data is very good. It should be noted that the analytical results are obtained by considering the mutual inductances relevant to the eigenvalues numbered by $i = 1$ and 2 (3). Namely, the mutual inductances between the parallel stems separated by a distance larger than $2S$ are neglected in the model. It is possible of course to fully take into account all these inductances, which in turn results in rigorous numerical calculations.

Table 2 Analytical results for the capacitance of the UMIs as compared to the ADS simulation results

No.	Turns	L, mm	W, mm	S, mm	ε_r	H, mm	C_{sim}	C_{anal}
1	12	20	0.4	0.2	2.2	0.8	0.787	0.722
2	10	20	0.4	0.2	4.6	0.8	0.719	0.852
3	10	20	0.4	0.2	9.6	1.6	1.417	1.191
4	15	20	0.4	0.2	9.6	1.6	1.513	1.786
5	25	9	0.6	0.3	9.6	1.6	1.509	1.189
6	25	12	0.6	0.3	9.6	1.6	1.054	0.974
7	25	18	0.6	0.3	4.6	0.8	1.337	1.461
8	25	12	0.5	0.2	4.6	0.8	1.739	1.827
9	23	10	0.4	0.2	3.38	0.8	0.815	0.758
10	23	10	0.4	0.1	3.38	0.8	0.813	0.968

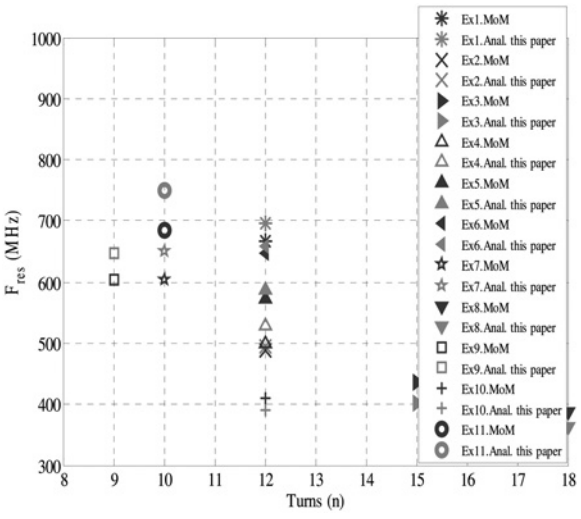

Fig. 5 *Comparison of ADS and analytically predicted resonant frequency for 11 different UMI*

Design parameters: $l = 20$ mm (Exs. 1, 2, 3, 5, 6, 7 and 11), $l = 25$ mm (Exs. 4, 8, 9 and 10), $W = 0.4$ mm (Exs. 1, 2, 3, 5, 6, 7 and 11), $W = 0.5$ mm (Exs. 9 and 10), $W = 0.6$ (Exs. 4 and 8), $S = 0.2$ mm (Exs. 1, 2, 3, 5, 6, 7, 9 and 11), and $S = 0.3$ mm (Exs. 4 and 8), $h = 0.8$ mm (Exs. 1, 4, 8, 9 and 11), and $h = 1.6$ mm (Exs. 2, 3, 5, 6 and 10), and $\varepsilon_r = 2.2$ (Exs. 1 and 6), $\varepsilon_r = 4.6$ (Exs. 4, 5, 8, 9 and 11), $\varepsilon_r = 9.6$ (Exs. 2, 3, 7 and 10)

3 Ungrounded interdigital capacitors

The geometry of an UIC comprised of 8 fingers, is shown in Fig. 6*a*. In this section, an accurate model for UICs is proposed and successfully validated through a comparison with the simulated results obtained using Agilent-ADS. Here, the interdigital capacitor is printed on a dielectric substrate with a thickness h and dielectric constant ε_r. A conceptual sketch of the UIC, which takes into account all the capacitive couplings between the fingers, is shown in Fig. 6*a*.

3.1 Analytical formula for C_{UIC}

The quasi-static circuit model associated with the UIC is depicted in Fig. 6*b*. C_{UIC} is generally owing to the capacitance between the neighbouring fingers, whereas the inductance L_{UICs} is proportional to the total magnetic energy stored in the interdigital resonator. Here, we assume that the finger width S, finger length L, and the separation distance between neighbouring fingers G, do not vary from finger to finger, as shown in Fig. 6*a*.

As revealed in Fig. 6*a*, the total distributed capacitance of the UIC is composed of three different components, namely, C_1, C_2 and C_{2s}. The closed form expressions for each component can be obtained by using the conformal mapping method. The first distributed capacitance C_1 is calculated as

$$C_1 = \varepsilon_0\varepsilon_{\mathrm{eff}_1}\frac{K(k_{01})}{K(k'_{01})}L \tag{13}$$

where L is the finger length, K (k_i) is the complete elliptic integral of the first kind and

$$k_{01} = \sqrt{1-\left(\frac{G}{G+S}\right)^2}, \quad \varepsilon_{\mathrm{eff}_1} = 1 + q_1\frac{\varepsilon_r - 1}{2}$$

$$k'_{i1} = (1-k_{i1}^2)^{0.5} \quad i = 0, 1$$

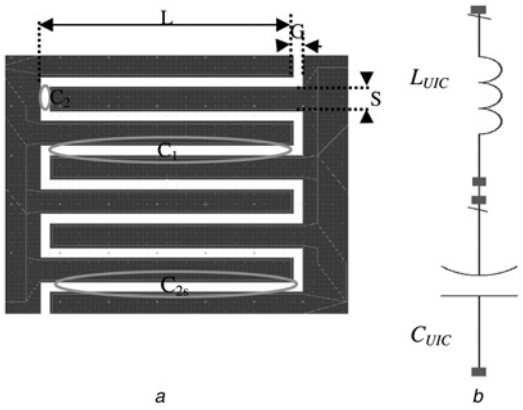

Fig. 6 *Ungrounded interdigital capacitors*

a Schematic of a UIC with eight fingers and its design parameters
b Quasi-static equivalent circuit of the UIC depicted in *a*

$$q_1 = \frac{K(k_{11})}{K(k'_{11})}\frac{K(k'_{01})}{K(k_{01})}$$
$$k_{11} = \sqrt{1 - \left(\frac{\sinh((\pi G/)/4h)}{\sinh((\pi(G+S)/4h))}\right)^2} \quad (14)$$

By extending the theory presented in [18], the capacitance of the outer edge of the interdigital capacitor can be calculated as

$$C_{2s} = 2\varepsilon_0\varepsilon_{\text{eff}2\,s}\frac{K(k'_{02s})}{K(k_{02s})}L \quad (15)$$

where

$$k_{02s} = \frac{G}{G+2S}, \quad \varepsilon_{\text{eff}\,2s} = 1 + q_{12s}\frac{\varepsilon_r - 1}{2}$$
$$k'_{i2s} = (1 - k^2_{i2s})^{0.5} \quad i = 0, 1$$
$$q_{12s} = \frac{K(k'_{i2s})}{K(k_{12s})}\frac{K(k_{02s})}{K(k'_{02s})} \quad (16)$$
$$k_{12s} = \frac{\sinh((\pi G)/4h)}{\sinh((\pi(G+2S)/4h))}$$

The gap capacitance at the end of each finger can be obtained by [19]

$$C_2 = 2\varepsilon_0\varepsilon_{\text{eff}\,1}\frac{K(k_{01})}{K(k'_{01})}L_{\text{ext}} \quad (17)$$

where

$$L_{\text{ext}} = \frac{A}{12.5\times10^{-6}}\left[-4\times10^{-6}\left(\frac{S}{2A}\right)^2 + 9\times10^{-6}\left(\frac{S}{2A}\right) + 8\times10^{-6}\right] \times\left[1 + \left(\frac{A}{G+A}\right)^3\right], \quad A = \frac{S+2G}{4} \quad (18)$$

Finally, the total distributed capacitance of the ungrounded interdigital capacitor composed of n fingers can be determined as follows

$$C_{\text{UIC}} = (n-2)C_1 + C_{2s} + nC_2 \quad (19)$$

As for L_{UMIs}, we assume here that the higher-order effects (i.e. capacitive coupling between the non-adjacent fingers) are negligible. The behaviour of the distributed capacitance (C_{UIC}) as a function of the number of fingers for different finger widths/gaps is shown in Fig. 7. When the number of fingers is increased, the capacitance value increases. Moreover, for a constant number of fingers, the capacitance value increases as the finger width increases or gap width decreases.

3.2 Analytical formula for L_{UIC}

We now consider the total inductance of the ungrounded interdigital capacitor, L_{UIC}. To simplify the analytical formulation, one can assume that the small end-gaps are shorted, because of the quasi-static approximation. Considering the self-inductance of each individual strip

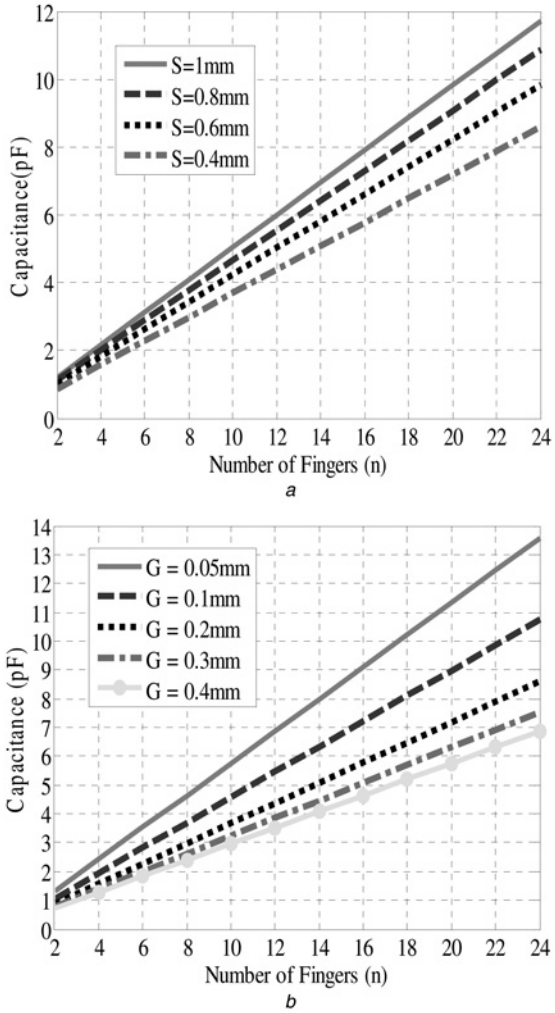

Fig. 7 *Total capacitance of UIC as a function of the number of fingers of the UIC, n*

a For different finger widths; $G = 0.2$ mm, $l = 10$ mm and $\varepsilon_r = 3.38$
b For different finger gaps; $S = 0.4$ mm, $l = 10$ mm and $\varepsilon_r = 3.38$

(finger) with a length of L, the inductance matrix of the UIC can be determined as follows

$$L_{\text{UIC}} = \begin{pmatrix} L_{11} & L_{12} & \dots & L_{1(n)} \\ L_{21} & L_{22} & \dots & L_{2(n)} \\ \vdots & \vdots & \dots & \vdots \\ L_{(n)1} & L_{(n)2} & \dots & L_{(n)(n)} \end{pmatrix}_{(n)\times(n)} \quad (20)$$

where L_{ii} is the self-inductance of each finger given in (1), and L_{ij} $(i \neq j)$ is the mutual-inductance between any two fingers given in (2). The equivalent inductance of the UIC can then be written as

$$L_{\text{UIC}} = \frac{1}{\sum_{i=1}^{i=n}\sum_{j=1}^{j=n}\Gamma_{ij}} \quad (21)$$

where n is the number of fingers and Γ is the inverse of the inductance matrix. The behaviour of the equivalent inductance of the UIC as a function of the number of fingers for different finger widths and gap widths is shown in Fig. 8. As can be seen, when the number of fingers is increased, the inductance value decreases. Moreover, for a constant number of fingers, the inductance value increases

doi: 10.1049/iet-map.2011.0436

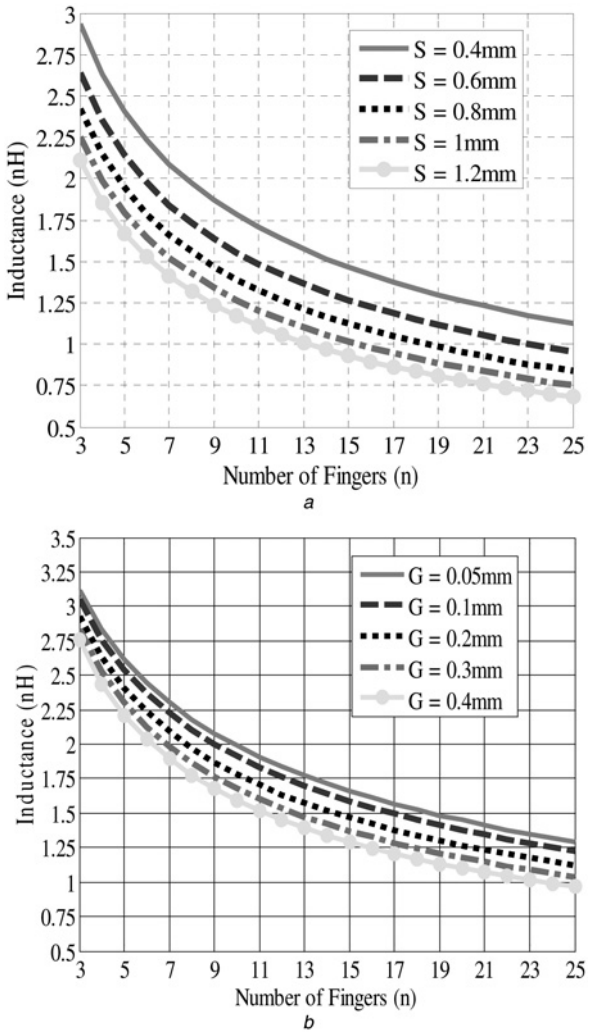

Fig. 8 *Total inductance of UIC as a function of the number of fingers of the UIC, n*

a For different finger widths; $G = 0.2$ mm, $l = 10$ mm and $\varepsilon_r = 3.38$
b For different finger gaps; $S = 0.4$ mm, $l = 10$ mm and $\varepsilon_r = 3.38$

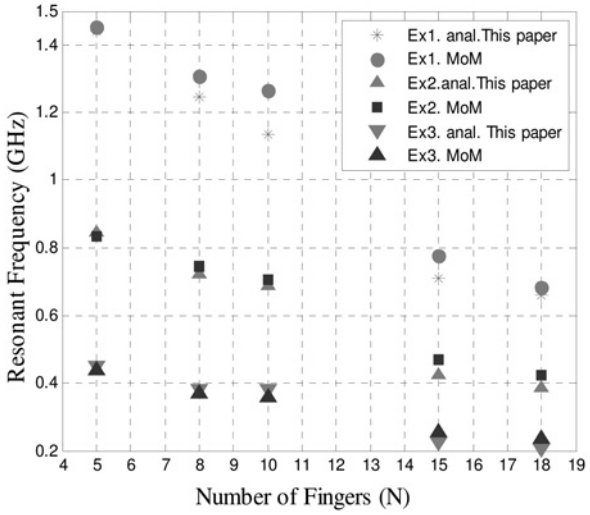

Fig. 9 *Resonant frequency of the UIC as a function of the number of fingers n*

Comparison between ADS simulation results and analytical results obtained using the proposed quasi-static model for three different UICs. Data Ex.1: $L = 10$ mm, $S = 0.4$ mm, $G = 0.1$ mm, $h = 0.5$ mm and $\varepsilon_r = 3.38$; data Ex.2: $L = 15$ mm, $S = 0.6$ mm, $G = 0.2$ mm, $h = 0.8$ mm, and $\varepsilon_r = 4.6$; data Ex.3: $L = 20$ mm, $S = 0.8$ mm, $G = 0.3$ mm, $h = 1.6$ mm and $\varepsilon_r = 9.6$

as the finger width or gap-width decreases. Finally, according to (19) and (21), the resonant frequency of the UIC can be written as

$$f_{\text{res}_{\text{UIC}}} = \frac{1}{2\pi\sqrt{L_{\text{UIC}}C_{\text{UIC}}}} \tag{22}$$

Some examples, comparing the resonant frequencies of the UICs obtained using the proposed quasi-static model with those obtained using Agilent-ADS, are shown in Fig. 9. As can be seen, the agreement between the quasi-static model and the simulated data is reasonably good.

4 UCRLH metamaterial sample and quality factor of UMIs and UICs

An UCRLH sample, which consists of a series combination of n UICs and n UMIs, is a practical approach to realise the LH materials. The equivalent circuit model of a planar UCRLH structure in microstrip technology constituted of UICs and UMIs is shown in Fig. 10. Considering Bloch–Floquet's theorem, the dispersion relation of the UCRLH

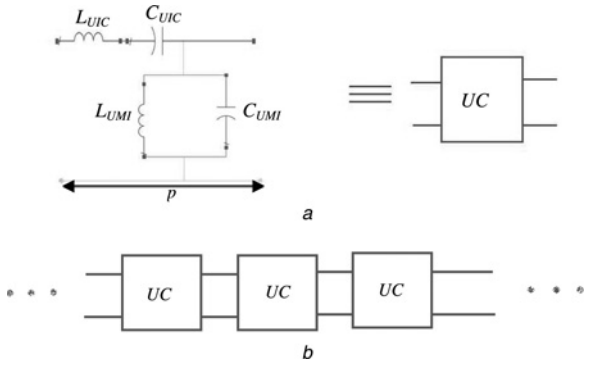

Fig. 10 *Equivalent circuit model of an UCRLH structure*

a Unit cell
b Periodic network implementation

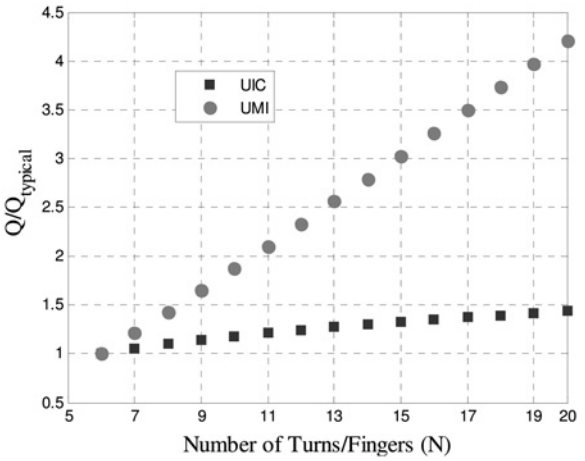

Fig. 11 *Quality factor comparison of UMIs/UICs with different number of turns/fingers*

Quality factor is normalised to a typical UMI/UIC (Q_{typical}) with the same design parameters and $n = 6$. Design parameters of the UMIs are: $l = 20$ mm, $W = 0.6$ mm, $S = 0.3$ mm, $h = 0.8$ mm and $\varepsilon_r = 3.38$ and design parameters of UICs are: $L = 20$ mm, $G = 0.2$ mm, $S = 0.8$ mm, $h = 0.8$ mm and $\varepsilon_r = 3.38$

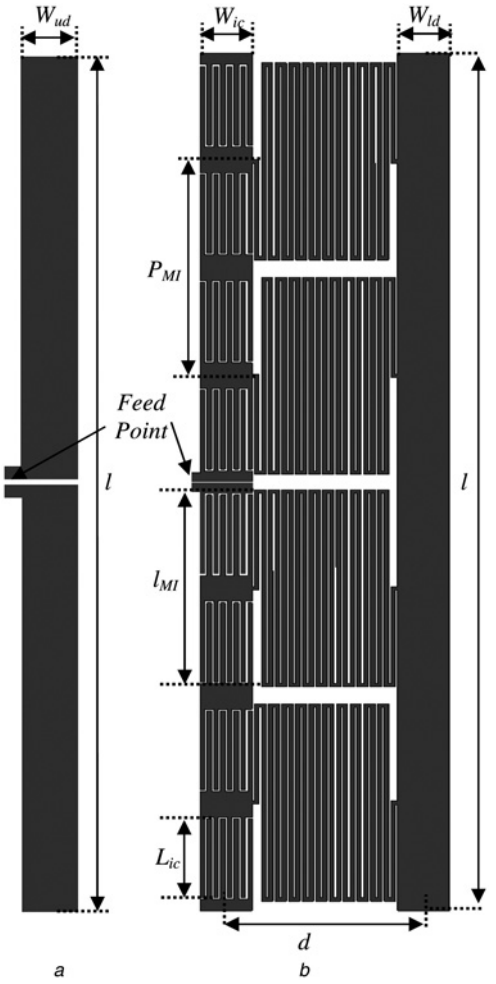

Fig. 12 *Schematic of*

a Unloaded printed dipole antenna
b UCRLH loaded printed dipole antenna: $l = 100$ mm, $P_{MI} = 25$ mm, $d = 16.6$ mm, $W_{ld} = W_{ic} = 4.6$ mm, $L_{ic} = 9.2$ mm, $l_{MI} = 23$ mm, $W_{ud} = 0.05$ h, number of UCRLH cells = 4, line width of UIC = 0.4 mm, gap width of UIC = 0.1 mm, line width of UMI = 0.4 mm, gap width of UMI =0.2 mm

transmission line (TL) of Fig. 10 can be easily found to be

$$\beta = \frac{1}{p} \times \cos^{-1}\left\{1 - \frac{1}{2}\left[\frac{1}{\omega^2 L_{\mathrm{UIC}} C_{\mathrm{UIC}}} + \omega^2 L_{\mathrm{UMI}} C_{\mathrm{UMI}} - \left(\frac{L_{\mathrm{UMI}}}{L_{\mathrm{UIC}}} + \frac{C_{\mathrm{UMI}}}{C_{\mathrm{UIC}}}\right)\right]\right\} \quad (23)$$

where ω is the angular frequency, and p is the periodicity of the unit cell. C_{UMI} and L_{UMI} are, respectively, the equivalent capacitance and inductance of the UMI whereas C_{UIC} and L_{UIC} are, respectively, the equivalent capacitance and inductance of the UIC. Therefore according to the analytical

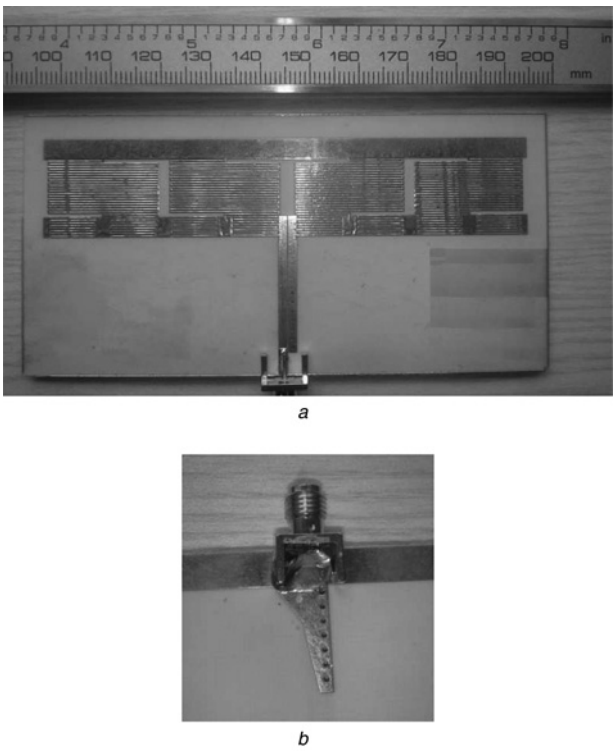

Fig. 13 *Photograph of a prototype printed dipole antenna loaded with UCRLH metamaterials*

a Front view
b Back view (balun configuration)

formulas presented in the previous sections, one can easily compute the dispersion relation, $\beta(\omega)$.

One of the interesting applications of UCRLH structures is to load printed antennas and microstrip filters in order to realise miniaturised microwave devices. However, it should be borne in mind that the operating bandwidth of the inclusions is restricted as the electrical dimensions of the inclusions decrease. Therefore the dimensions of the inclusions are a result of a trade-off between the achievable miniaturisation and bandwidth. Further insight is sought through the study of the quality factor Q, of UCRLH structures, which is inversely proportional to the operating bandwidth. The quality factor of UMIs, like other parallel LC resonant circuits [20], is approximately proportional to the square root of the capacitance and inversely proportional to the square root of the inductance, whereas the quality factor of the UICs is proportional to the square root of the inductance and inversely proportional to the square root of the capacitance. The relative quality factors (Q/Q_{typical}) of both the UMIs and UICs as a function of the number of turns/fingers (n) are plotted in Fig. 11. As can be seen, the quality factor of the inclusions increases as the number of the turns/fingers increases.

Table 3 A comparison between analytical and simulated resonant frequency

No.	L_R, nH	C_L, pF	L_L, nH	C_R, pF	$fr_{analysed}$, GHz	$fr_{simulated}$, GHz
Ex.1	2.1845	3.9392	63.545	0.96879	0.2518	0.261
Ex.2	2.1725	3.0767	71.733	0.6926	0.306	0.275
Ex.3	2.1725	4.3014	71.733	0.76811	0.234	0.235

For $m = -1$; Ex.1: $\varepsilon_r = 3.38$, $h = 0.8$ mm, $G_{\mathrm{UIC}} = 0.1$ mm, $S_{\mathrm{UMI}} = 0.1$ mm; Ex.2: $\varepsilon_r = 2.2$, $h = 0.8$ mm, $G_{\mathrm{UIC}} = 0.2$ mm, $S_{\mathrm{UMI}} = 0.2$ mm; Ex.3: $\varepsilon_r = 3.55$, $h = 0.8$ mm, $G_{\mathrm{UIC}} = 0.2$ mm, $S_{\mathrm{UMI}} = 0.2$ mm

doi: 10.1049/iet-map.2011.0436

Owing to the removal of the ground plane, the UMIs and UICs are generally low resistance structures. Thus, the quality factors of the UMIs and UICs are generally high resulting in a lower bandwidth.

5 Printed dipole antenna loaded with UCRLH structures

The first application of UCRLH materials was proposed by Hall *et al.* [13], where properties of the UCRLH structures were used to develop a design methodology for a miniaturised printed dipole antenna. In this section, the printed dipole antenna proposed in [13] has been thoroughly investigated both analytically and experimentally. The configuration of the UCRLH loaded dipole is shown in Fig. 12. The design parameters of the antenna are also provided in the caption of Fig. 12. The excitation of negative resonance modes of the printed dipole antenna is a unique feature of the UCRLH loaded dipole that can lead to interesting potential applications. The operational mechanism of the present antenna has been investigated in [13]. In this section, the resonance frequencies of the UCRLH loaded dipole are analytically calculated as a function of the resonant frequency of the unloaded dipole f_{ru}, C_{UIC}, L_{UIC}, C_{UMI} and C_{UMI}. Using (23), the resonant frequency of the negative mode of order m can be obtained as follows

$$b_1\omega_m^4 - b_2\omega_m^2 + 1 = 0 \quad \text{where } b_1 = L_R L_L C_R C_L$$
$$b_2 = BL_L C_L \quad \text{and} \quad f_m = \omega_m/2\pi \tag{24}$$

where

$$B = 2(1 - \cos(|A|)) + \left(\frac{L_R}{L_L} + \frac{C_R}{C_L}\right)$$
$$A = \frac{2\pi \mathrm{pm} f_{\mathrm{ru}}\sqrt{\varepsilon_{\mathrm{eff}}}}{C} \quad m = -1,\ -3,\ -5,\ \ldots \tag{25}$$

where f_{ru} denotes the resonant frequency of the unloaded-dipole. Equation (24) has four distinct roots of which only one is acceptable, corresponding to the resonance frequency of the fundamental negative mode. A comparison between the analytically predicted and numerically predicted resonance frequencies of different UCRLH loaded dipoles is reported in Table 3. Here, we just change the substrate permittivity and other design parameters are kept the same as in the caption of Fig. 12. As can be seen, the agreement between the simulated data and the theoretical data is good. Finally, a prototype of the UCRLH loaded dipole is fabricated to validate the theoretical results. Fig. 13 shows a photograph of the fabricated antenna. The antenna is printed on a substrate with dielectric constant of 3.38 and thickness of 0.8 mm. Fig. 14 shows the measured reflection coefficient of the antenna as compared with the simulation results and theoretical data. It can be seen that the measured and simulated resonant frequencies of the UCRLH loaded dipole are in good agreement with the theoretical predictions. The measured and simulated co- and cross-polarised radiation patterns of the loaded antenna at the resonant frequency corresponding to $m = -1$ are also shown in Fig. 15.

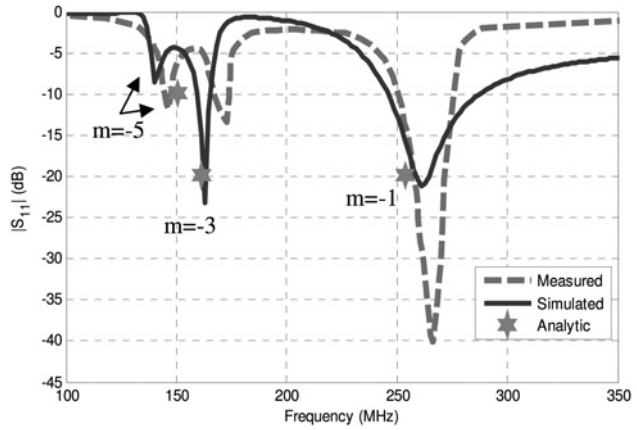

Fig. 14 *Reflection coefficient of the UCRLH loaded printed dipole*

6 Conclusion

The design of UCRLH metamaterials composed of UMIs and UICs is presented. Efficient quasi-static models and exact analytical formulas, for both the UMIs and the UICs, are proposed. The theory is compared with different measurement and simulation results resulting in a very good

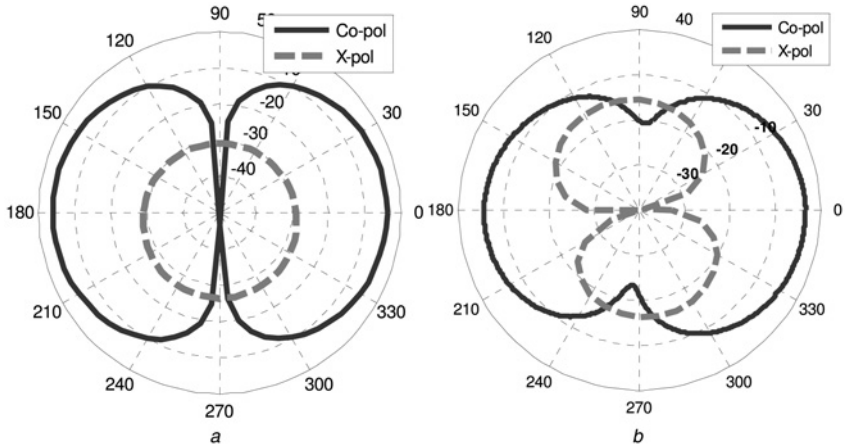

Fig. 15 *Co- and cross-polarised radiation patterns of the UCRLH loaded dipole in E-plane*

a Simulated
b Measured

agreement between them. The parametric studies on the UICs and the UMIs were conducted to obtain engineering guidelines for the UCRLH metamaterial designs. Finally, the behaviour of a printed dipole loaded with UCRLH structures is investigated both theoretically and numerically.

7 References

1 Daly, D.A., Knight, S.P., Caulton, M., Ekholdt, R.: 'Lumped elements in microwave integrated circuits', *IEEE Trans. Microw. Theory Tech.*, 1967, **15**, pp. 713–721

2 Hong, J.S., Lancaster, M.J.: 'Microstrip filters for RF/microwave applications' (John Wiley & Sons, 2001)

3 Alley, G.D.: 'Interdigital capacitors and their application to lumped-element microwave integrated circuits', *IEEE Trans. Microw. Theory Tech.*, 1970, **18**, pp. 1028–1033

4 Acuna, J.E., Rodriguez, J.L., Obelliero, F.: 'Design of meander line inductors on printed circuit boards', *Int. J. RF Microw. Comp. Aid. Eng.*, 2001, **11**, pp. 219–230

5 Acuna, J.E., Rodriguez, J.L., Obelliero, F.: 'Modeling double-side printed meander-line inductors on printed circuit boards', *Int. J. RF Microw. Comp. Aid. Eng.*, 2003, **13**, pp. 105–112

6 Caloz, C., Okabe, H., Iwai, T., Itoh, T.: 'Transmission line approach of left-handed (LH) materials'. USNC/URSI National Radio Science Meeting, San Antonio, TX, June 2002, vol. 1, p. 39

7 Caloz, C., Itoh, T.: 'Transmission line approach of left-handed (LH) structures and microstrip realization of a low-loss broadband LH filter', *IEEE Trans. Antennas Propag.*, 2004, **52**, (5), pp. 1159–1166

8 Caloz, C., Sanada, A., Itoh, T.: 'Microwave applications of transmission-line based negative refractive index structures'. Proc. Asia-Pacific Microwave Conf., Seoul, Korea, November 2003, vol. 3, pp. 1708–1713

9 Lai, A., Caloz, C., Itoh, T.: 'Transmission line based metamaterials and their microwave applications', *Microw. Mag.*, 2004, **5**, (3), pp. 34–50

10 Sanada, A., Caloz, C., Itoh, T.: 'Characteristics of the composite right/left handed transmission lines', *IEEE Microw. Wirel. Compon. Lett.*, 2004, **14**, (2), pp. 68–70

11 Caloz, C., Itoh, T.: 'Electromagnetic metamaterials: transmission line theory and microwave applications' (Wiley-Intersience, Hoboken, NJ, 2006)

12 Iizuka, H., Hall, P.S.: 'Orthogonally polarised dipole antenna using left handed transmission lines'. Proc. 36th European Microwave Conf., 2006

13 Iizuka, H., Hall, P.S.: 'A left-handed dipole antenna and their implementations', *IEEE Trans. Antennas Propag.*, 2007, **55**, (5), pp. 1246–1253

14 Hall, P.S., Liu, Q.: 'Dipoles and loop antennas with left handed loading'. Loughborough Antennas & Propagation Conf., 2008

15 Ruehli, A.E.: 'Inductance calculations in a complex integrated circuit environment', *IBM J. Res. Dev.*, 1972, **16**, pp. 470–481

16 Wu, R.B., Kuo, C.N., Chang, K.K.: 'Inductance and resistance computations for three-dimensional multiconductor interconnection structures', *IEEE Tans. Microw. Theory Tech.*, 1992, **40**, (2), pp. 263–271

17 Grover, F.W.: 'Inductance calculations: working formulas and tables, Van Nostrand' (D. Van Nostrand, New York, 1946)

18 Ghione, G., Naldi, C.: 'Analytical formulas for coplanar lines in hybrid and monolithic MICs', *Electron. Lett.*, 1984, **20**, (4), pp. 159–181

19 Beilenhoff, K., Klingbeil, H., Heinrich, W., Hartnagel, H.L.: 'Open and short circuits in coplanar MMIC's', *IEEE Trans. Microw. Theory Tech.*, 1993, **41**, pp. 1534–1537

20 Bilotti, F., Toscano, A., Vegni, L.: 'Design of spiral and multiple split-ring resonators for the realization of miniaturized metamaterial samples', *IEEE Trans. Antennas Propag.*, 2007, **55**, (8), pp. 2258–2267

doi: 10.1049/iet-map.2011.0436